

Equilibrium and nonequilibrium applications of lattice-gas models in electrochemistry

Per Arne Rikvold^{a,b,c}, Gregory Brown^{a,b}, M. A. Novotny^{b,d}, Andrzej Wieckowski^e

^a *Center for Materials Research and Technology and Department of Physics,
Florida State University, Tallahassee, FL 32306-3016, USA*

^b *Supercomputer Computations Research Institute,
Florida State University, Tallahassee, FL 32306-4052, USA*

^c *Department of Fundamental Sciences, College of Integrated Human Studies,
Kyoto University, Kyoto 606, Japan*

^d *Department of Electrical Engineering, FAMU-FSU College of Engineering,
Tallahassee, FL 32310-6046, USA*

^e *Department of Chemistry and Frederick Seitz Materials Research Laboratory,
University of Illinois, Urbana, IL 61801, USA*

We discuss applications of statistical-mechanical lattice-gas models to study static and dynamic aspects of electrochemical adsorption. The strategy developed to describe specific systems includes microscopic model formulation, calculation of zero-temperature phase diagrams, numerical simulation of thermodynamic and structural quantities at nonzero temperatures, and estimation of effective, lateral interactions. We briefly review earlier work, including studies by Monte Carlo simulation of the adsorption of urea on Pt(100). As an illustrative example, we discuss in some detail recent applications to the underpotential deposition of Cu with sulfate on Au(111). Experimental and numerical results are included for equilibrium coverages and voltammetric currents at slow potential sweep rates, and new results from dynamic Monte Carlo simulations are presented. In particular, we present simulated results for current transients far from equilibrium, following sudden changes in the electrode potential.

Keywords: Electrochemical adsorption; Underpotential deposition; Lattice-gas models; Computer simulations; Nonequilibrium statistical mechanics

I. INTRODUCTION

The recent confluence of electrochemistry and surface science has occasioned a two-way exchange of experimental and theoretical techniques between these previously disparate disciplines. Here we discuss electrochemical applications of a theoretical method adapted from surface science: computational, statistical-mechanical lattice-gas modeling. In Secs. 2 and 3 we briefly review some earlier equilibrium and near-equilibrium work [1–6], including an application to the electrosorption of urea on Pt(100) [7–9], and we briefly summarize a strategy to obtain effective, lateral adsorbate-adsorbate interactions by comparing model results with experiments performed at or near equilibrium. More extensive reviews of this work can be found in Refs. [9,10].

As an illustration of the approach, in Sec. 4 we give a “case study” of a particular system: the underpotential deposition (UPD) of Cu with sulfate on Au(111) [9,11–18]. First we review the results of a recent Monte Carlo (MC) study of equilibrium coverages and voltammetric currents at very low potential sweep rates [17]. This discussion is followed by an extension of the model to study its *dynamical* behavior following a sudden change in the electrode potential. In particular, we present new simulation results for the time-dependent coverages, voltammetric currents, and microscopic adsorbate structures. The reasonable agreement with recent current-transient measurements by Hölzle et al. [19] is encouraging.

II. LATTICE-GAS MODELS OF SUBMONOLAYER CHEMISORPTION

The models we discuss are defined by the two-component lattice-gas Hamiltonian [1–3,7–9,17],

$$\mathcal{H} = - \sum_n \sum_{\langle ij \rangle}^{(n)} \left[\Phi_{AA}^{(n)} c_i^A c_j^A + \Phi_{AB}^{(n)} (c_i^A c_j^B + c_i^B c_j^A) + \Phi_{BB}^{(n)} c_i^B c_j^B \right] + \mathcal{H}_3 - \sum_i [\bar{\mu}_A c_i^A + \bar{\mu}_B c_i^B]. \quad (1)$$

Here $c_i^X \in \{0,1\}$ is the local occupation variable for species X; $\sum_{\langle ij \rangle}^{(n)}$ and \sum_i run over all n th-neighbor bonds and over all adsorption sites, respectively; $\Phi_{XY}^{(n)}$ denotes the effective lateral XY pair interaction through an n th-neighbor bond;

\sum_n runs over the interaction ranges; and \mathcal{H}_3 contains multi-particle interactions. The change in electrochemical potential when one X particle is adsorbed is $-\bar{\mu}_X$. Particular systems differ in their binding-site geometries and the values and ranges of the lateral interactions. The thermodynamic density conjugate to $\bar{\mu}_X$ is the surface coverage,

$$\Theta_X = N^{-1} \sum_i c_i^X, \quad (2)$$

where N is the number of surface unit cells. The mapping between the electrochemical potentials in the lattice-gas Hamiltonian, $\bar{\mu}_X$, and the bulk activities $[X]$ and electrode potential E is accomplished through the relation,

$$\bar{\mu}_X = \mu_X^0 + RT \ln ([X]/[X]^0) - z_X F E, \quad (3)$$

where R is the molar gas constant, T is the absolute temperature, F is Faraday's constant, z_X is the effective electrovalence of X, and μ_X^0 and $[X]^0$ are reference values which include the local binding energies.

The interactions in Eq. (1) are *effective* interactions mediated through several channels. The mechanisms include interactions between the adsorbate and the substrate electron structure, adsorbate-induced deformations of the substrate, interactions with the fluid electrolyte, and (screened) electrostatic interactions. Theoretical and computational methods are not yet sufficiently advanced to obtain these multi-source interactions from first principles. A method to estimate them on the basis of comparison between lattice-gas calculations and experiments is summarized in the next section.

III. VOLTAMMETRY AND ADSORBATE STRUCTURE NEAR EQUILIBRIUM

In the limit of vanishing potential sweep rate, the voltammetric current per unit cell is the time derivative of the charge transported across the interface during the adsorption/desorption process:

$$q = -e(z_A \Theta_A + z_B \Theta_B), \quad (4)$$

where e is the elementary charge. The current density is easily obtained in terms of the lattice-gas response functions, $\partial\Theta_X/\partial\bar{\mu}_Y$, as

$$i = eF \left\{ z_A^2 \frac{\partial\Theta_A}{\partial\bar{\mu}_A} + 2z_A z_B \frac{\partial\Theta_B}{\partial\bar{\mu}_A} + z_B^2 \frac{\partial\Theta_B}{\partial\bar{\mu}_B} \right\} \frac{dE}{dt}. \quad (5)$$

A strategy has been developed to determine the effective interactions [8,9], providing a practical alternative to “first-principles” methods. This consists in fitting thermodynamic and structural model predictions from zero-temperature phase diagrams and numerical simulations at room temperature to experiments, considering a variety of physical quantities. Obviously, this also has its problems. The potential number of parameters is large, and there is no guarantee that a minimal set of interactions is unique. Nevertheless, previous lattice-gas studies of electrochemical systems indicate that when all available experimental information is consistently included, this approach has considerable predictive power. The steps in the modeling strategy can be summarized as follows.

1. Use prior theoretical and experimental knowledge about the substrate lattice structure and lattice constant and the shapes and sizes of the adsorbate particles to formulate a specific lattice-gas model.
2. Use experimental information about adsorbate coverages and adlayer structure to determine the adsorbate phases.
3. Perform a group-theoretical ground-state calculation to construct a ground-state diagram (zero-temperature phase diagram) and determine a minimal set of effective interactions consistent with the observed adsorbate phases.
4. At nonzero temperatures, the thermodynamic and structural properties of the lattice-gas model constructed through steps 1–3 can be studied by various analytical and numerical methods, depending on the quantities of interest and the complexity of the Hamiltonian. In the applications discussed here, we have mostly used numerical MC simulation. This method has the advantage that it is quite accurate, even for two-dimensional systems [20], and relatively straightforward to implement.
5. The finite-temperature properties obtained in Step 4 should be used to refine the effective interactions by comparison with the available experiments, or by obtaining additional experimental data for such comparison. Steps 4 and 5 should be iterated until satisfactory agreement between model and experiment is achieved.

Examples of the application of the approach sketched above to the chemisorption of small adsorbate particles on single-crystal electrodes include the adsorption of urea on Pt(100) from perchloric acid [7–9] and the UPD of Cu on

Au(111) from sulfuric acid [13,17,18]. Both systems exhibit a prominent peak sharpening in the cyclic voltammogram (CV) when a small concentration of the adsorbate (urea or copper ions) is added to the electrolyte. Whereas the urea/Pt(100) system develops a single CV peak [21], in copper UPD two peaks are exhibited [11,12]. The voltammetric changes are much weaker or absent when the same substances are adsorbed on other crystal planes of the same metals, indicating that they depend crucially on the geometric fit between the adsorbates and the surface. These peaks are associated with adsorbate phase transitions [12,22].

Below we consider in detail simulations of some equilibrium and nonequilibrium aspects of the UPD of Cu with sulfate on Au(111).

IV. UPD OF CU WITH SULFATE ON AU(111)

A. Near-equilibrium aspects

In underpotential deposition (UPD), a monolayer of one metal is electrochemically adsorbed onto another in a range of electrode potentials more positive than those where bulk deposition occurs. The UPD of Cu on Au(111) in sulfuric acid has been intensively studied, both experimentally (see discussion of the literature in Ref. [17]) and theoretically [13–18]. The most striking feature in CV experiments on this system is the appearance of two peaks, 100~150 mV apart, upon addition of Cu^{2+} ions to the sulfuric-acid electrolyte [11,12]. Typical CV profiles are shown in Fig. 1(a), together with simulation results. In the potential range between the peaks, the adsorbate layer has a $(\sqrt{3} \times \sqrt{3})$ structure with $2/3$ ML Cu and $1/3$ ML sulfate [13–18,23], first proposed by Huckaby and Blum (HB) [13]. Typical experimental and simulated coverages are shown versus electrode potential in Fig. 1(b).

The lattice-gas model used by Zhang et al. [17] has interactions through fourth-nearest neighbors (see also Ref. [18]). Sulfate is assumed to coordinate the triangular Au(111) surface through three of its oxygen atoms, with the fourth S-O bond away from the surface. This gives a triangular “footprint” that reasonably matches the Au(111) unit cell. The adsorption sites for the Cu and sulfate are assumed to lie on the same triangular lattice. The model is illustrated in Fig. 2.

Adsorption isotherms and CV currents at room temperature were obtained from MC heat-bath simulations on $L \times L$ triangular lattices with $L=30$ and 45. The simulated quantities were adjusted to obtain overall agreement with the experimental data as described in Sec. III. The experimental and simulated CV currents and coverages are shown together in Figs. 1(a) and 1(b), respectively. The resulting estimates for the effective lateral interactions are given in the caption of Fig. 2.

It has been experimentally observed [24,25] that sulfate is adsorbed on top of the Cu monolayer at negative potentials. Zhang et al. used a simple mean-field approximation for the sulfate coverage in this second layer: $\Theta_S^{(2)} = \alpha \Theta_C (\frac{1}{3} - \Theta_S)$, where α is a phenomenological constant. Since the transfer of sulfate between the gold and copper surfaces does not involve an oxidation/reduction process, the total charge transport per unit cell during the adsorption/desorption process becomes

$$q = -e[z_S(\Theta_S + \Theta_S^{(2)}) + z_C\Theta_C], \quad (6)$$

which modifies the CV current given in Eq. (5) in a straightforward way [17]. The effective electrovalences, z_S and z_C , must be determined from experiments. Zhang et al. obtained the values, $z_C \approx +1.7$ and $z_S \approx -1.1$ [17], using data from Omar et al. [26]. To within the statistical errors, these estimates agree with independent experimental results by Shi and Lipkowski [24,25]. Comparing with values proposed by Blum et al. [18] based on a theoretical mean-field calculation, we observe that their estimate for z_C is about 35% less positive than those obtained by Zhang et al. and Shi and Lipkowski, while there is no statistically significant disagreement about z_S .

The ground-state diagram corresponding to the interactions obtained in Ref. [17] is shown in Fig. 3. For large negative $\bar{\mu}_S$, only copper adsorption is possible. Similarly, in the limit of large positive $\bar{\mu}_S$ and large negative $\bar{\mu}_C$, the zero-temperature phase is the $(\sqrt{3} \times \sqrt{3})_0^{1/3}$ sulfate phase [we denote phases as $(X \times Y)_{\Theta_C^S}^{\Theta_S}$] characteristic of the hard-hexagon model corresponding to the infinitely repulsive nearest-neighbor sulfate-sulfate interaction $\Phi_{SS}^{(1)}$ [6,13–15]. (See Fig. 4.)

The potential scan path corresponding to the CV profile and coverages shown in Fig. 1 is indicated by the dotted line labeled “1” in the ground-state diagram, Fig. 3. Starting from the negative end, we consider a scan proceeding in the direction of positive electrode potential (upper left to lower right in Fig. 3). Near the CV peak at approximately 200 mV vs. Ag/AgCl (labeled Peak # 2 in Fig. 1), the sulfate begins to compete with copper for the adsorption sites, resulting in a third of the copper desorbing and being replaced by sulfate. Due to the strong effective attraction between the copper and sulfate adparticles, the mixed $(\sqrt{3} \times \sqrt{3})_{2/3}^{1/3}$ phase is formed (see Fig. 4). In this phase, which

extends through the entire potential region between the two CV peaks, Cu forms a honeycomb lattice with a sulfate molecule at the center of each cell. As the CV peak at approximately 300 mV (labeled Peak # 1 in Fig. 1) is reached, most of the copper is desorbed within a narrow potential range. As it is thus deprived of the stabilizing influence of the coadsorbed copper, the sulfate is almost completely desorbed.

Dynamical aspects of the phase transition at Peak # 1 are discussed in Sec. IV B below.

B. Current transients far from equilibrium

Whereas the preceding discussion presents a near-equilibrium theory, with voltammetric currents at slow potential sweep rates obtained from adsorption isotherms, analysis of fast sweeps or potential-step experiments requires a true nonequilibrium treatment. In the early-time regime, mean-field rate equations can be satisfactory [27,28]. However, for later times, when coalescence of adsorbate islands may become important, this approach is no longer necessarily reliable [29–31]. For systems in which the phases involved are ordered, the microscopic adlayer structure and the dynamical details of the adsorption and lateral diffusion processes become important, even at early times. We have therefore initiated a study of the dynamics of electrochemical adsorption by numerical simulation of microscopic models. Here we present some preliminary results of this work.

We consider the model for UPD of Cu with sulfate on Au(111), discussed in Sec. IV A above, with the parameters that were obtained by Zhang et al. through comparison with near-equilibrium experiments [17]. We focus on the current transients following sudden changes of the electrode potential across the discontinuous phase transition at Peak # 1, and we discuss our results in the light of recent experiments by Hölzle et al. [19].

The model dynamics is implemented through a refusal-free dynamic MC algorithm [32,33], in which the transition rates are determined by free energies of activation (“free-energy barriers”) [34]. The transition rate from a microscopic configuration a to a different configuration b is taken to be

$$k_{a \rightarrow b} = k' \exp \left(-\frac{\Delta G_{a \rightarrow b}^*}{RT} \right), \quad (7)$$

where k' is a standard rate and $\Delta G_{a \rightarrow b}^*$ is the free energy of activation for the particular transition. The eventual approach to equilibrium is ensured through the detailed-balance condition,

$$\Delta G_{a \rightarrow b}^* - \Delta G_{b \rightarrow a}^* = \mathcal{H}(b) - \mathcal{H}(a), \quad (8)$$

where $\mathcal{H}(a)$ and $\mathcal{H}(b)$ are the values of the lattice-gas Hamiltonian in Eq. (1), corresponding to the two configurations. In these exploratory simulations we have taken the free-energy barrier associated with adsorption of particles of species X to depend linearly on the electrochemical potential $\bar{\mu}_X$ (and thus on the electrode potential) through a Butler-Volmer type relation [19,34],

$$\Delta G_{\text{ads } X}^*(\bar{\mu}_X) = \Delta G_{\text{ads } X}^*(0) - \alpha \bar{\mu}_X, \quad (9)$$

and for simplicity we set the transfer coefficient $\alpha=1/2$. The barriers associated with lateral diffusion are taken to be independent of the electrochemical potentials and, except insofar as they must satisfy Eq. (8), of the local geometry of the adsorbate layer.

The time unit used in the simulations, called MC steps per site (MCSS), is determined by the standard rate constants and is expected to be proportional to the physical time. The proportionality constant must be determined by physico-chemical arguments and comparison with the experimentally observed timescales.

We simulated positive-going and negative-going potential-step experiments along the scan path labeled “3” in Fig. 3, where Peak # 1 is centered at approximately 260 mV vs. Ag/AgCl [17]. Before the positive-going steps, the model was equilibrated in the ordered $(\sqrt{3} \times \sqrt{3})_{2/3}^{1/3}$ phase, 15 mV on the negative side of the transition. At time $t=0$ the potential was changed instantaneously to a final value a distance ΔE past the transition. Following Hölzle et al., we used $\Delta E = 24, 28, 31$, and 33 mV. For the negative-going steps we equilibrated in the disordered low-coverage phase, 45 mV on the positive side of the transition, followed at $t=0$ by a step into the ordered-phase region with $\Delta E = -15$ mV. Since the second-layer sulfate coverage is negligible in this potential region [see Fig. 1(b)], in this study we only considered first-layer effects.

The simulated current transients [in units of elementary charges per Au(111) unit cell and MCSS] are shown in Fig. 5. We used systems of size 60×60 with periodic boundary conditions. The results were averaged over 100 trials for each value of ΔE , and the current data were smoothed using a running average over seven time points. As we discuss in detail below, the experimentally observed asymmetry with respect to potential steps of opposite sense is captured by our dynamical model.

The current transients for the positive-going potential steps, which are shown in Fig. 5(a), are characterized by a sharp current spike at early times, followed later by a second, broader maximum. The experimentally observed trends with respect to changes in ΔE are also reproduced, both for the locations and the sizes of the peaks. For the negative-going steps, no such two-peaked structure is observed. Instead, like in the experiments, a monotonically decreasing current is seen. This behavior is shown in Fig. 5(b).

The surface coverages, Θ_C and Θ_S , are shown versus time for positive-going steps in Figs. 6(a) and 6(b), respectively. Comparison of these results with Fig. 5(a) shows that the early-time current peak is almost entirely due to desorption of Cu. Only as Θ_C reaches a “metastable” value in the 0.4–0.5 ML range, does the sulfate start to desorb at a significant rate. At later times the relaxation appears to follow the nucleation-and-growth dynamics characteristic of the decay of a metastable phase [19,27,35]. The evolution of the spatial structure with time is illustrated by MC “snapshots” in Fig. 7. The growth of islands of the equilibrium low-coverage phase is quite apparent. A detailed investigation of the time dependence in the late-time regime, including the effective “Avrami exponent” [19,27] and its dependence on the free-energy barriers, will be presented at a later date [36].

The situation following a negative-going step is quite different. As seen in Fig. 8, Cu is rapidly adsorbed to a coverage of approximately 1/3 ML, which produces the large current at early times. The snapshots in Fig. 9 [in particular Fig. 9(b)] indicate that this structure is globally disordered, but *locally* has the symmetry of the Cu-only $(\sqrt{3} \times \sqrt{3})_{1/3}^0$ phase. For the particular potential steps used here, the energy of this phase lies between those of the mixed phase and the disordered low-coverage phase. The subsequent approach towards the mixed, ordered equilibrium phase requires the removal of a large number of domain walls by lateral diffusion and is consequently very slow. Again, a detailed investigation of this dynamics and its dependence on the model parameters will be presented later [36].

V. CONCLUSIONS

In this paper we have briefly reviewed some earlier applications of statistical-mechanical lattice-gas models to electrochemical adsorption problems. This approach, which was originally transferred from “traditional” surface science, has proven to be a useful and versatile tool in the study of multicomponent chemisorption in electrochemical systems near thermodynamic equilibrium.

Following this brief review, we presented preliminary results from a new application of the lattice-gas approach to dynamical phenomena far from equilibrium. In particular, we considered a dynamic extension of a model for UPD of Cu with sulfate on Au(111), originally introduced by Huckaby and Blum [13]. We used an extension of this model, with parameters obtained by Zhang et al. [9,17] through comparison of simulation results to experiments at or near equilibrium. To this we added activated dynamics including adsorption, desorption, and lateral diffusion. Our simulated results for current transients in this system show encouraging, qualitative agreement with recent experiments by Hölzle et al. [19]. This agreement includes the prominent asymmetry between the transients observed in positive-going and negative-going potential-step experiments. Although our results leave many details for further study, we believe they open the door towards numerical investigations of a wide range of interesting dynamical phenomena in electrochemical systems.

ACKNOWLEDGMENTS

Research at Florida State University was supported by the Center for Materials Research and Technology and by the Supercomputer Computations Research Institute (under U.S. Department of Energy Contract No. DE-FC05-85-ER25000) and by U.S. National Science Foundation grants No. DMR-9315969 and DMR-9634873. P.A.R.’s stay at Kyoto University during part of the work reported here was supported by the Japan Foundation Center for Global Partnership Science Fellowship Program through U.S. National Science Foundation Grant No. INT-9512679. Research at The University of Illinois was supported by U.S. National Science Foundation grant No. CHE-9411184 and by the Frederick Seitz Materials Research Laboratory (under U.S. Department of Energy Contract No. DE-AC02-76-ER01198).

REFERENCES

-
- [1] P.A. Rikvold, J.B. Collins, G.D. Hansen and J.D. Gunton, *Surf. Sci.*, 203 (1988) 500.
 - [2] J.B. Collins, P. Sacramento, P.A. Rikvold and J.D. Gunton, *Surf. Sci.*, 221 (1989) 277.
 - [3] P.A. Rikvold and M.R. Deakin, *Surf. Sci.*, 294 (1991) 180.
 - [4] L. Blum, *Adv. Chem. Phys.*, 78 (1990) 171.
 - [5] D.A. Huckaby and L. Blum, *J. Chem. Phys.*, 92 (1990) 2646.
 - [6] L. Blum and D.A. Huckaby, *J. Chem. Phys.*, 94 (1991) 6887.
 - [7] M. Gamboa-Aldeco, P. Mrozek, C.K. Rhee, A. Wieckowski, P.A. Rikvold and Q. Wang, *Surf. Sci. Lett.*, 297 (1993) L135.
 - [8] P.A. Rikvold, M. Gamboa-Aldeco, J. Zhang, M. Han, Q. Wang, H.L. Richards and A. Wieckowski, *Surf. Sci.*, 335 (1995) 389.
 - [9] P.A. Rikvold, J. Zhang, Y.-E. Sung and A. Wieckowski, *Electrochim. Acta*, 41 (1996) 2175.
 - [10] P.A. Rikvold, *Electrochim. Acta*, 36 (1991) 1689.
 - [11] J.W. Schultze and D. Dickertmann, *Surf. Sci.*, 54 (1976) 489.
 - [12] M. Zei, G. Qiao, G. Lempfuhr and D.M. Kolb, *Ber. Bunsen Ges. Phys. Chem.*, 91 (1987) 3494.
 - [13] D.A. Huckaby and L. Blum, *J. Electroanal. Chem.*, 315 (1991) 255.
 - [14] L. Blum and D.A. Huckaby, *J. Electroanal. Chem.*, 375 (1994) 69.
 - [15] L. Blum, M. Legault and P. Turq, *J. Electroanal. Chem.*, 379 (1994) 35.
 - [16] D.A. Huckaby and L. Blum, *Langmuir*, 11 (1995) 4583.
 - [17] J. Zhang, Y.-S. Sung, P.A. Rikvold and A. Wieckowski, *J. Chem. Phys.*, 104 (1996) 5699.
 - [18] L. Blum, D.A. Huckaby and M. Legault, *Electrochim. Acta*, 41 (1996) 2207.
 - [19] M.H. Hölzle, U. Retter and D. M. Kolb, *J. Electroanal. Chem.*, 371 (1994) 101.
 - [20] A comparison of results of perturbative and nonperturbative calculations for one and the same two-dimensional lattice-gas model is given by P.A. Rikvold and M.A. Novotny, in L. Blum and F.B. Malik (Eds.), *Condensed Matter Theories*, Vol. 8, Plenum, New York, 1993, p 627.
 - [21] M. Rubel, C.K. Rhee, A. Wieckowski and P.A. Rikvold, *J. Electroanal. Chem.*, 315 (1991) 301.
 - [22] P.A. Rikvold and A. Wieckowski, *Phys. Scr.*, T44 (1992) 71.
 - [23] M.F. Toney, J.N. Howard, J. Richer, G.L. Borges, J.G. Gordon II, O.R. Melroy, D. Yee and L.B. Sorenson, *Phys. Rev. Lett.*, 75 (1995) 4472.
 - [24] Z. Shi and J. Lipkowski, *J. Electroanal. Chem.*, 365 (1994) 303.
 - [25] Z. Shi, S. Wu and J. Lipkowski, *Electrochim. Acta*, 40 (1995) 9.
 - [26] I.H. Omar, H.J. Pauling and K. Jüttner, *J. Electrochem. Soc.*, 140 (1993) 2187.
 - [27] M. Avrami, *J. Chem. Phys.*, 7 (1933) 1103; 8 (1940) 212; 9 (1941) 177.
 - [28] E. Bosco and S.K. Rangarajan, *J. Chem. Soc. Faraday Trans. 1*, 77 (1981) 1673.
 - [29] R.A. Ramos, P.A. Rikvold and M.A. Novotny, in Z. Fisk, L. Gor'kov, D. Meltzer and R. Schrieffer (Eds.), *Physical Phenomena at High Magnetic Fields II*, World Scientific, Singapore, 1996, p. 380.
 - [30] P.A. Rikvold, A. Wieckowski and R.A. Ramos, *Mater. Res. Soc. Symp. Proc. Ser.*, (1997), in press.
 - [31] R.A. Ramos, S.W. Sides, P.A. Rikvold and M.A. Novotny, in preparation.
 - [32] A.B. Bortz, M.H. Kalos and J.L. Lebowitz, *J. Comput. Phys.*, 17 (1975) 10.
 - [33] M.A. Novotny, *Computers in Physics*, 9 (1995) 46.
 - [34] See, e.g., A.J. Bard and L.R. Faulkner, *Electrochemical Methods: Fundamentals and Applications*, Wiley, New York, 1980.
 - [35] P.A. Rikvold and B.M. Gorman, in D. Stauffer (Ed.), *Annual Reviews of Computational Physics I*, World Scientific, Singapore, 1994, p. 149.
 - [36] G. Brown, P.A. Rikvold, M.A. Novotny and A. Wieckowski, in preparation.

FIGURE CAPTIONS

FIG. 1. UPD of Cu with sulfate on Au(111). Electrolyte composition: 1.0 mM CuSO_4 + 0.1 mM H_2SO_4 . (a): CV profiles, $dE/dt = 2\text{mV/s}$. Experimental (dot-dashed) and simulated (30×30 : solid; 45×45 : \times) current densities. (b): Simulated coverages of Cu (dashed), first-layer sulfate (dotted), and total sulfate (solid), together with corresponding Auger Electron Spectroscopy data (\square and \times with error bars, respectively). After Ref. [17].

FIG. 2. Lattice-gas model for the UPD of copper (C) on Au(111) in the presence of sulfate (S) [17]. The relative positions of copper (\bullet) and sulfate (\triangle) correspond to the effective interactions in Eq. (1). The numbers are the corresponding values of $\Phi_{XY}^{(I)}$, in kJ/mol. From Ref. [9].

FIG. 3. Ground-state diagram for the lattice-gas model of copper UPD on Au(111), shown in the $(\bar{\mu}_S, \bar{\mu}_C)$ plane. The effective interactions are given in Fig. 2. The solid lines represent zero-temperature phase boundaries. The dotted line labeled “1” represents the voltammetric scan path at room temperature, corresponding to the data shown in Fig. 1. The lines labeled “2” and “3” correspond to 5 mM and 0.2 mM Cu^{2+} with unchanged sulfate concentration, respectively. The end points of all three lines correspond to $E=120$ mV (upper left) and 420 mV (lower right) vs. Ag/AgCl. The solid diamonds indicate the positions of Peak # 1, and the solid squares indicate the positions of Peak # 2 in the simulated room-temperature CV currents. The phases are denoted as $(X \times Y)_{\Theta_C}^{\Theta_S}$. From Ref. [17].

FIG. 4. Ground-state configurations corresponding to the main phases in the ground-state diagram, Fig. 3. The adsorption sites are shown as \circ , and Cu and sulfate are denoted by \bullet and \triangle , respectively, as in Fig. 2. Adapted from Ref. [17].

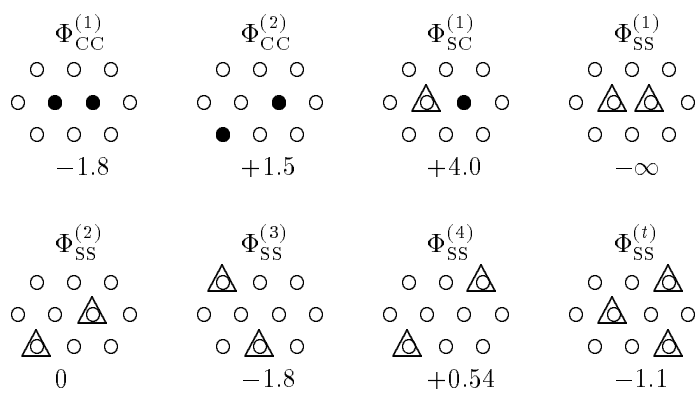
FIG. 5. Simulated current transients for potential steps ΔE of different magnitudes and directions across the phase transition at Peak # 1. The potential is changed along the scan path marked “3” in Fig. 3, and it takes the system between the ordered $(\sqrt{3} \times \sqrt{3})_{2/3}^{1/3}$ phase and the disordered low-coverage phase. The time t is given in MC steps per spin (MCSS), and the current density in elementary charges per Au(111) unit cell and MCSS. (a): Positive-going potential steps, $\Delta E = 24, 28, 31$, and 33 mV. (b): Negative-going potential step, $\Delta E = -15$ mV.

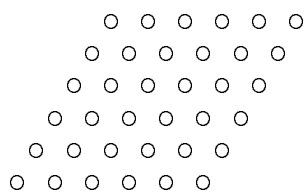
FIG. 6. Simulated adsorbate coverages versus time, following positive-going potential steps. The data correspond to the current transients shown in Fig. 5(a). (a): Copper. (b): Sulfate.

FIG. 7. “Snapshots” of configurations produced during a simulation of a 21×21 system following a positive-going potential step with $\Delta E = 24$ mV. Nucleation and growth of domains of the equilibrium low-coverage phase are apparent. The times shown are $t=0, 100, 300$, and 500 MCSS.

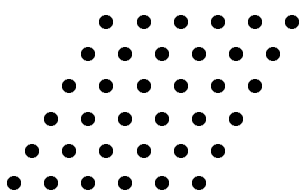
FIG. 8. Simulated adsorbate coverages versus time, following a negative-going potential step with $\Delta E = -15$ mV. The data correspond to the current transient shown in Fig. 5(b). Copper (solid); sulfate (dashed).

FIG. 9. “Snapshots” of configurations produced during a simulation of a 21×21 system following a negative-going potential step with $\Delta E = -15$ mV. Many locally ordered domains, separated by domain walls, are quickly formed. The subsequent equilibration requires the elimination of domain walls by lateral diffusion and is consequently very slow. The times shown are $t=0, 10, 200$, and 1000 MCSS.

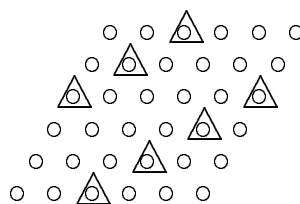




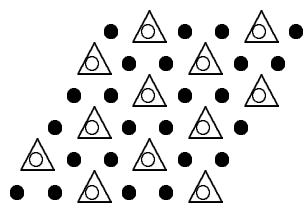
$$(1 \times 1)_0^0$$



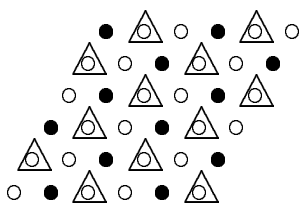
$$(1 \times 1)_1^1$$



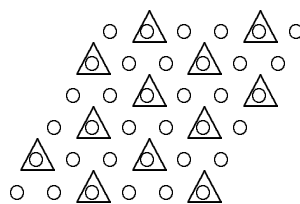
$$(\sqrt{3} \times \sqrt{7})_0^{1/5}$$



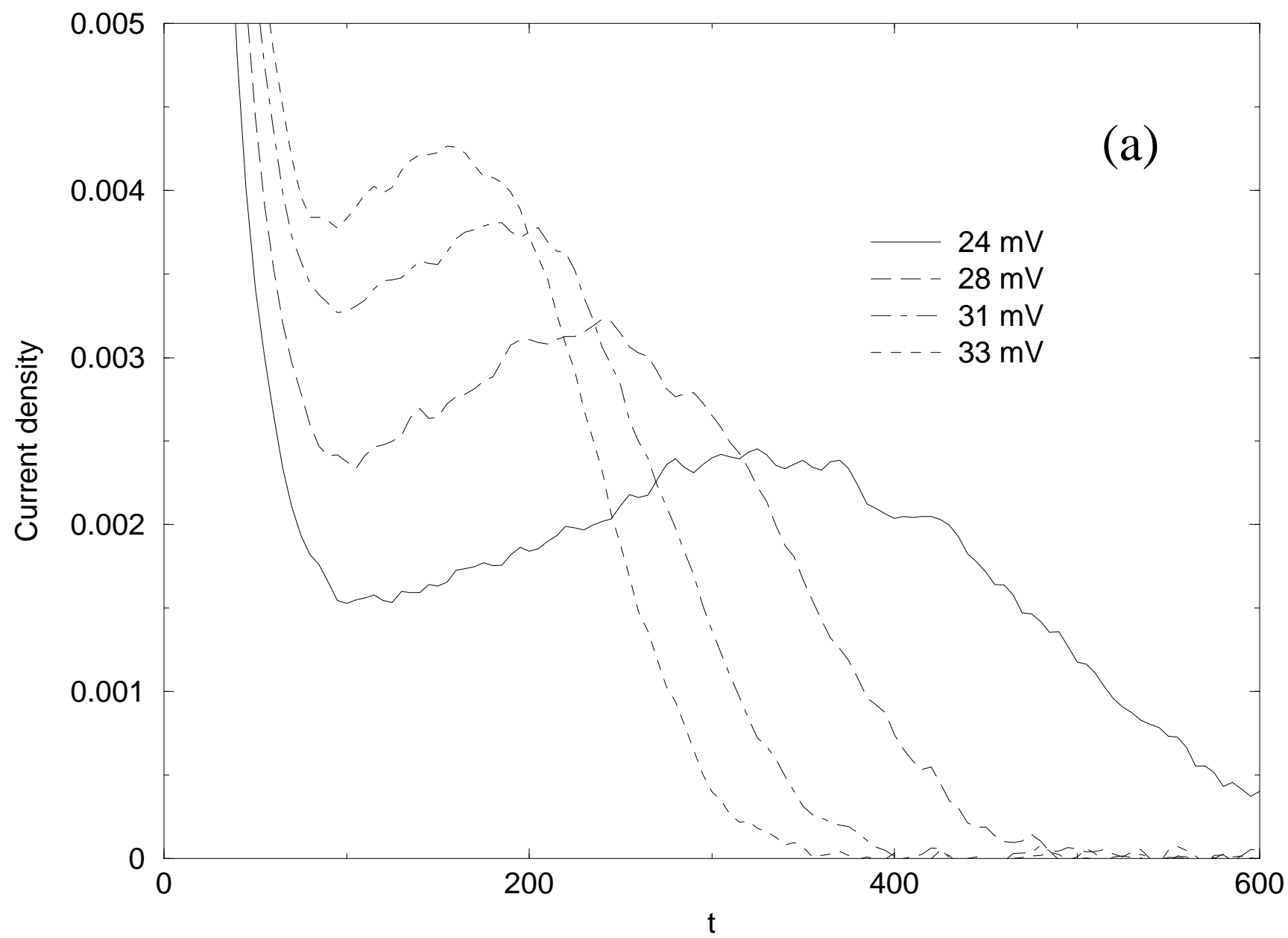
$$(\sqrt{3} \times \sqrt{3})_{2/3}^{1/3}$$

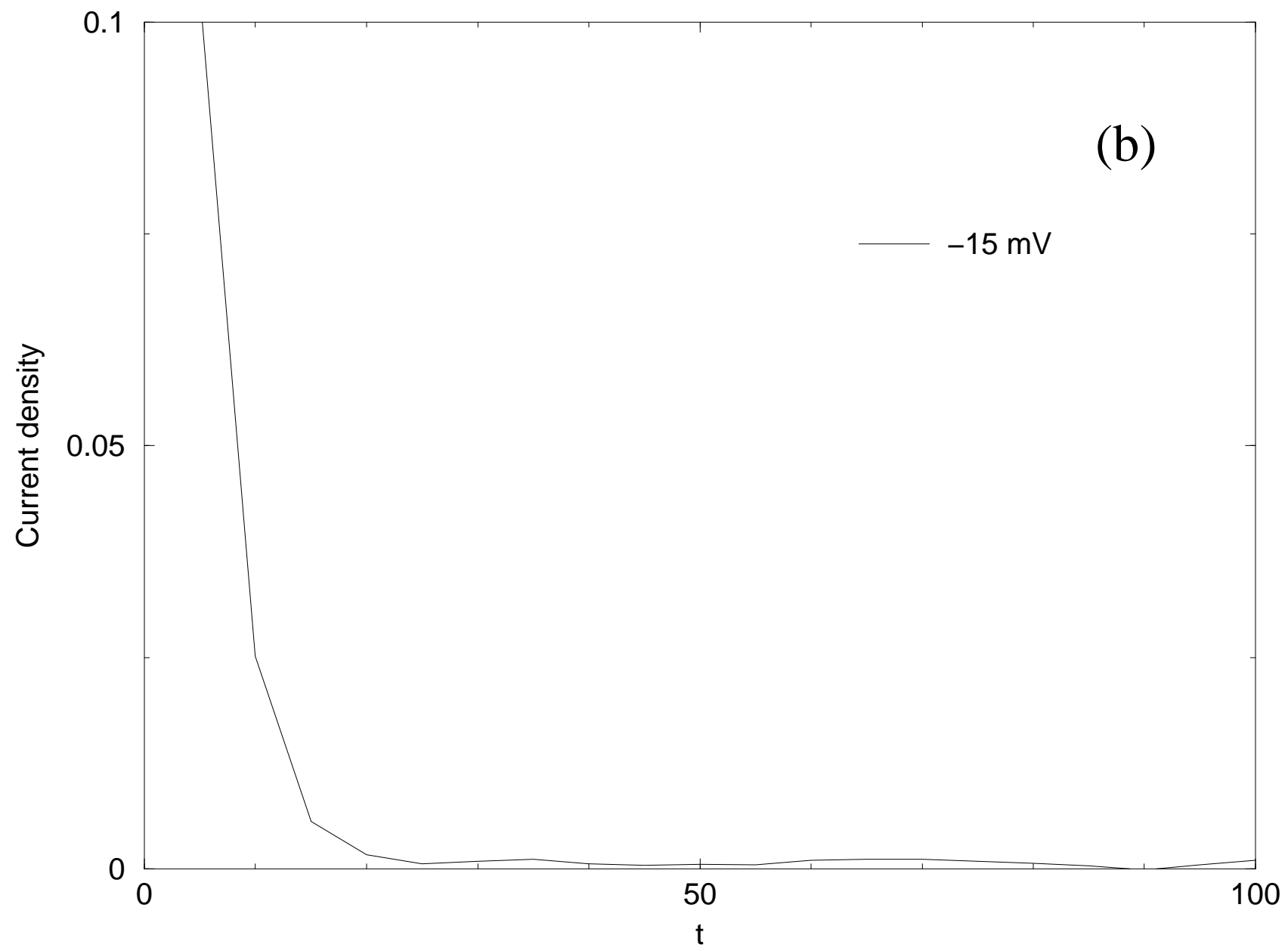


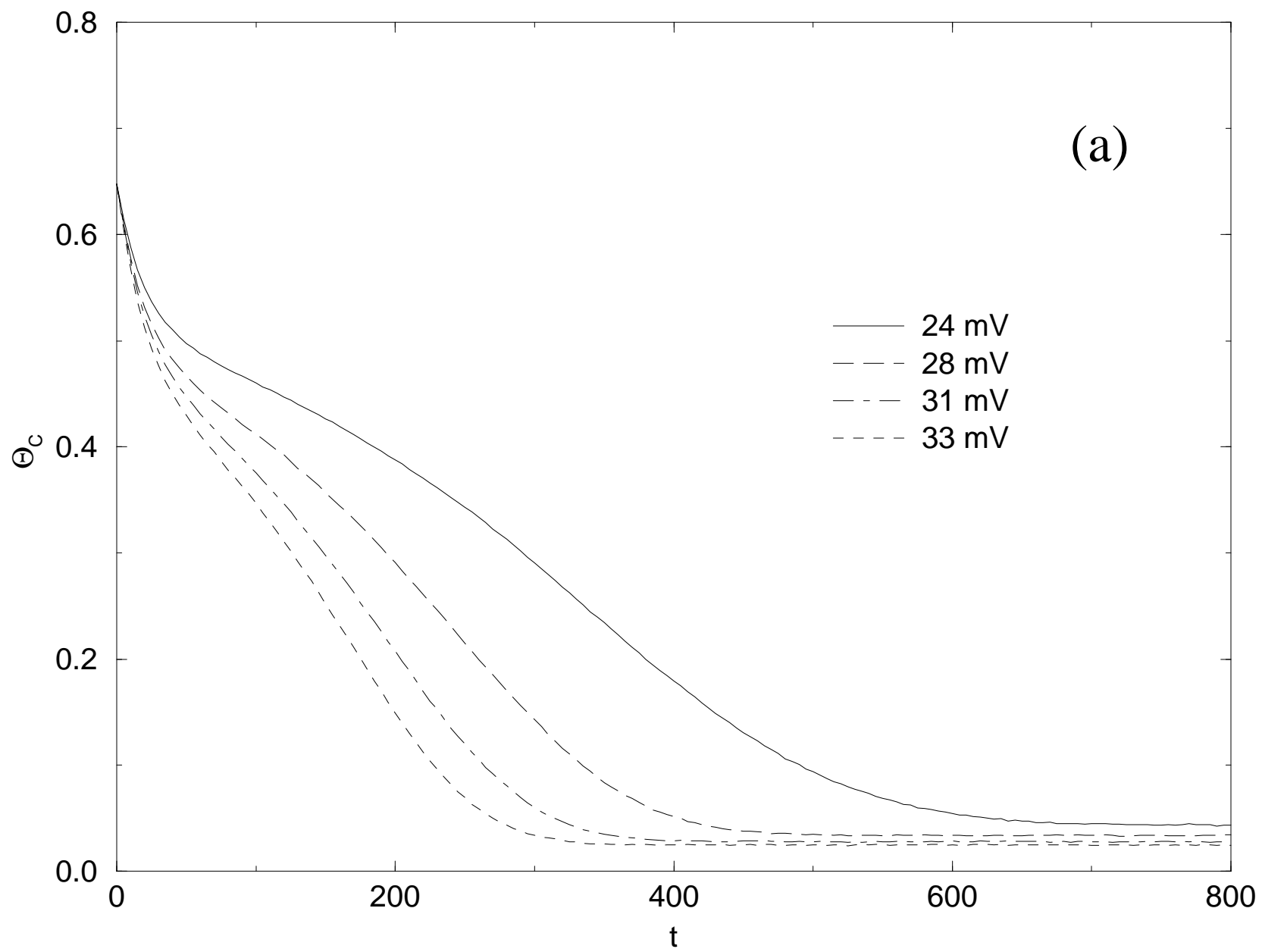
$$(\sqrt{3} \times \sqrt{3})_{1/3}^{1/3}$$

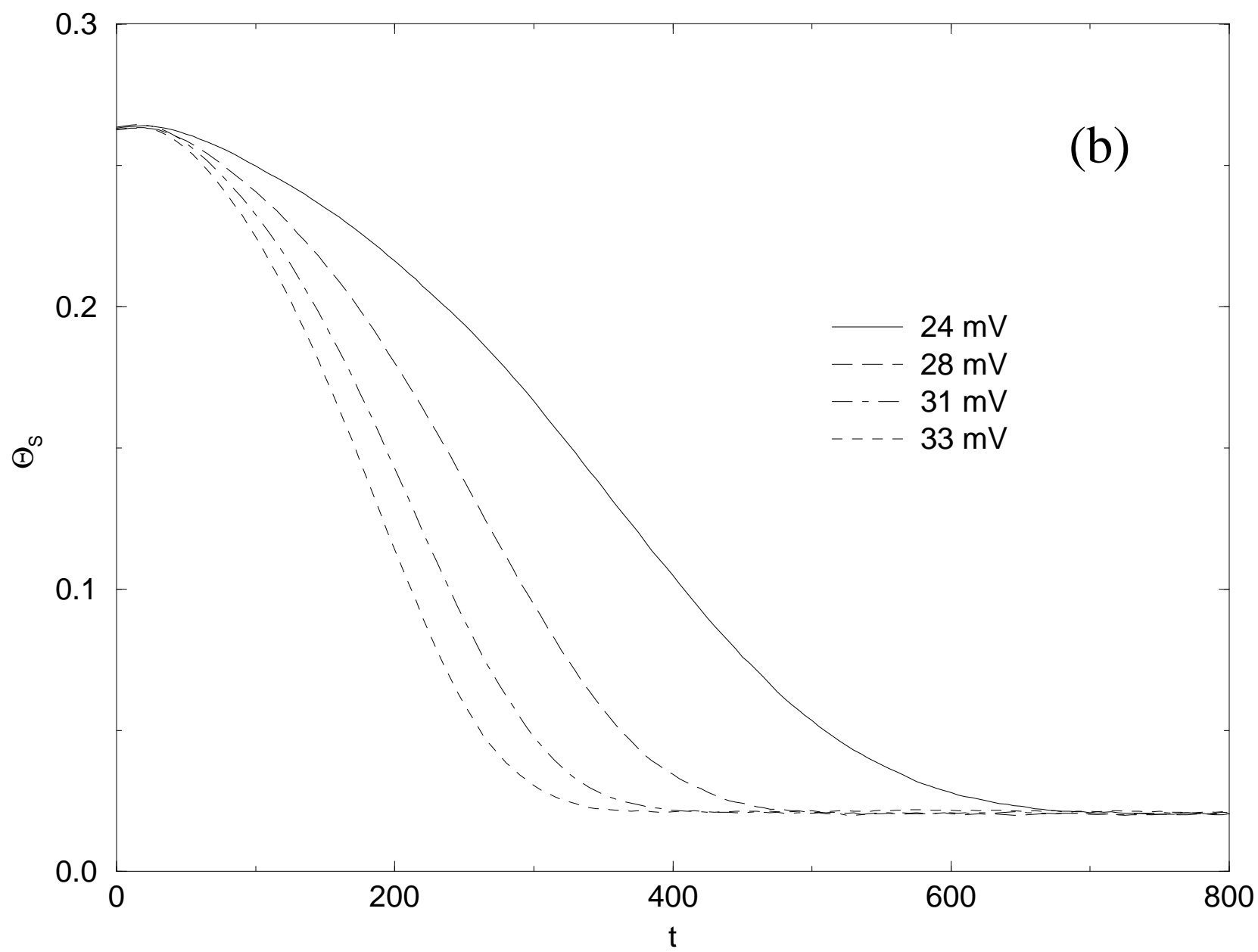


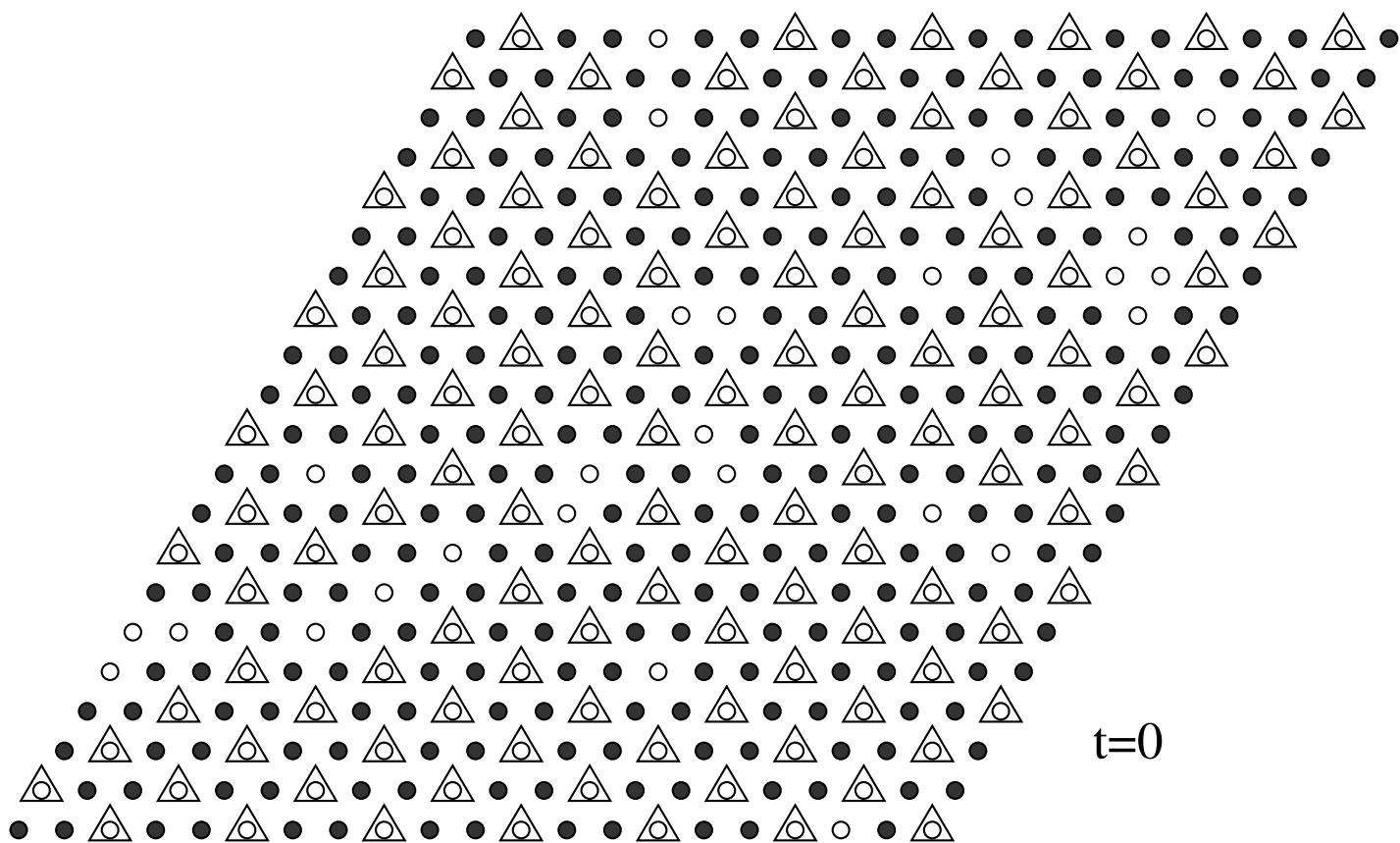
$$(\sqrt{3} \times \sqrt{3})_0^{1/3}$$

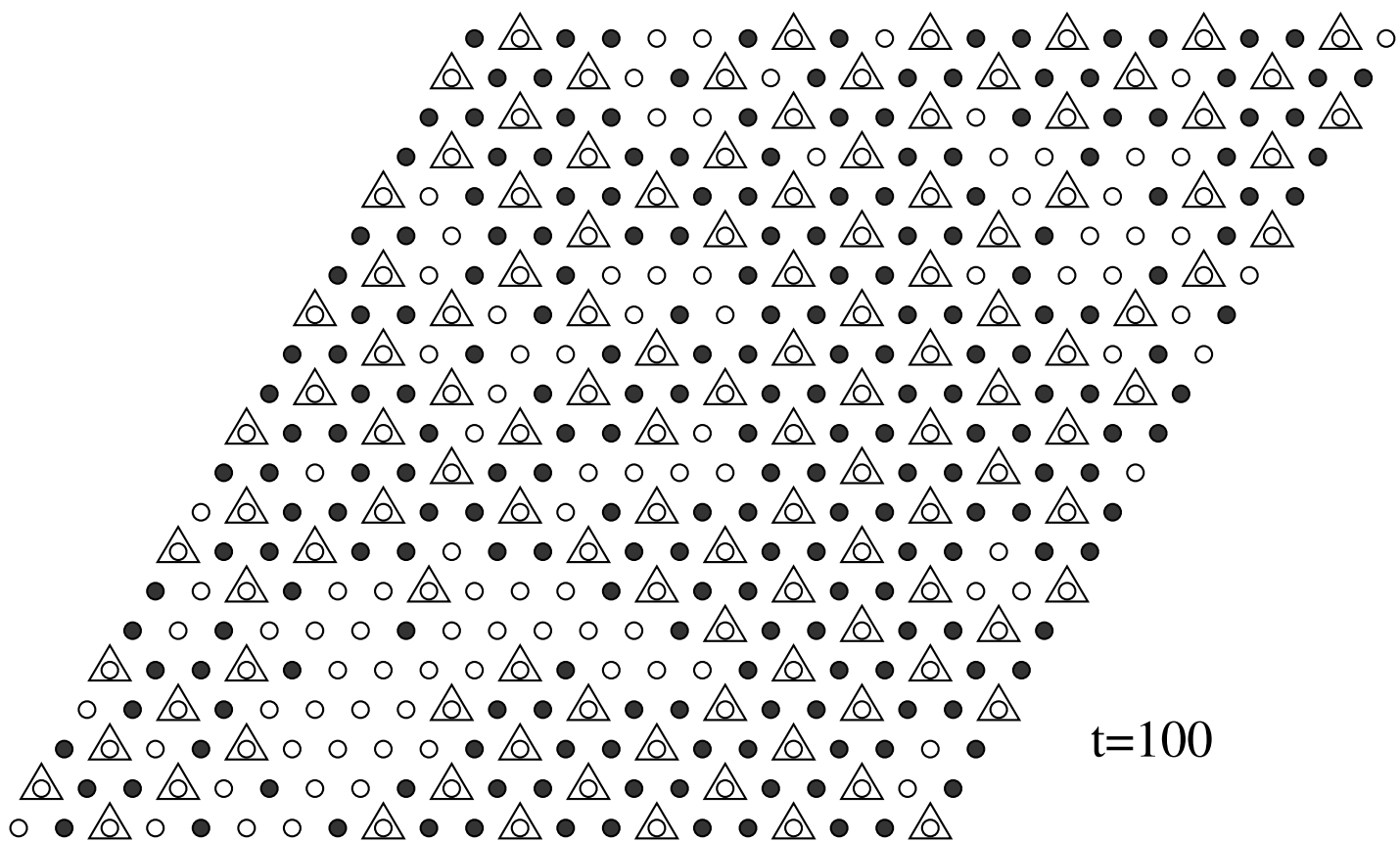


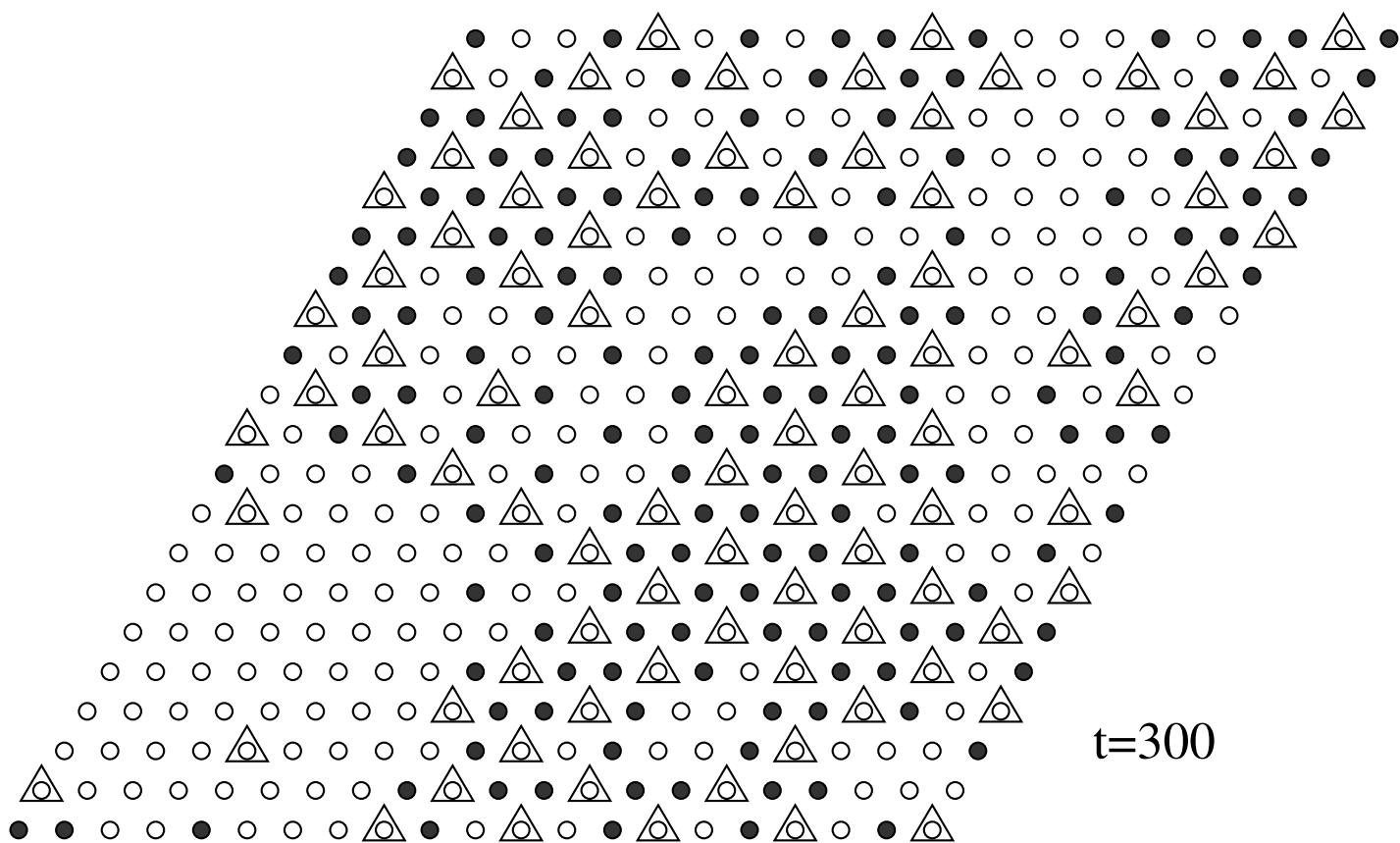




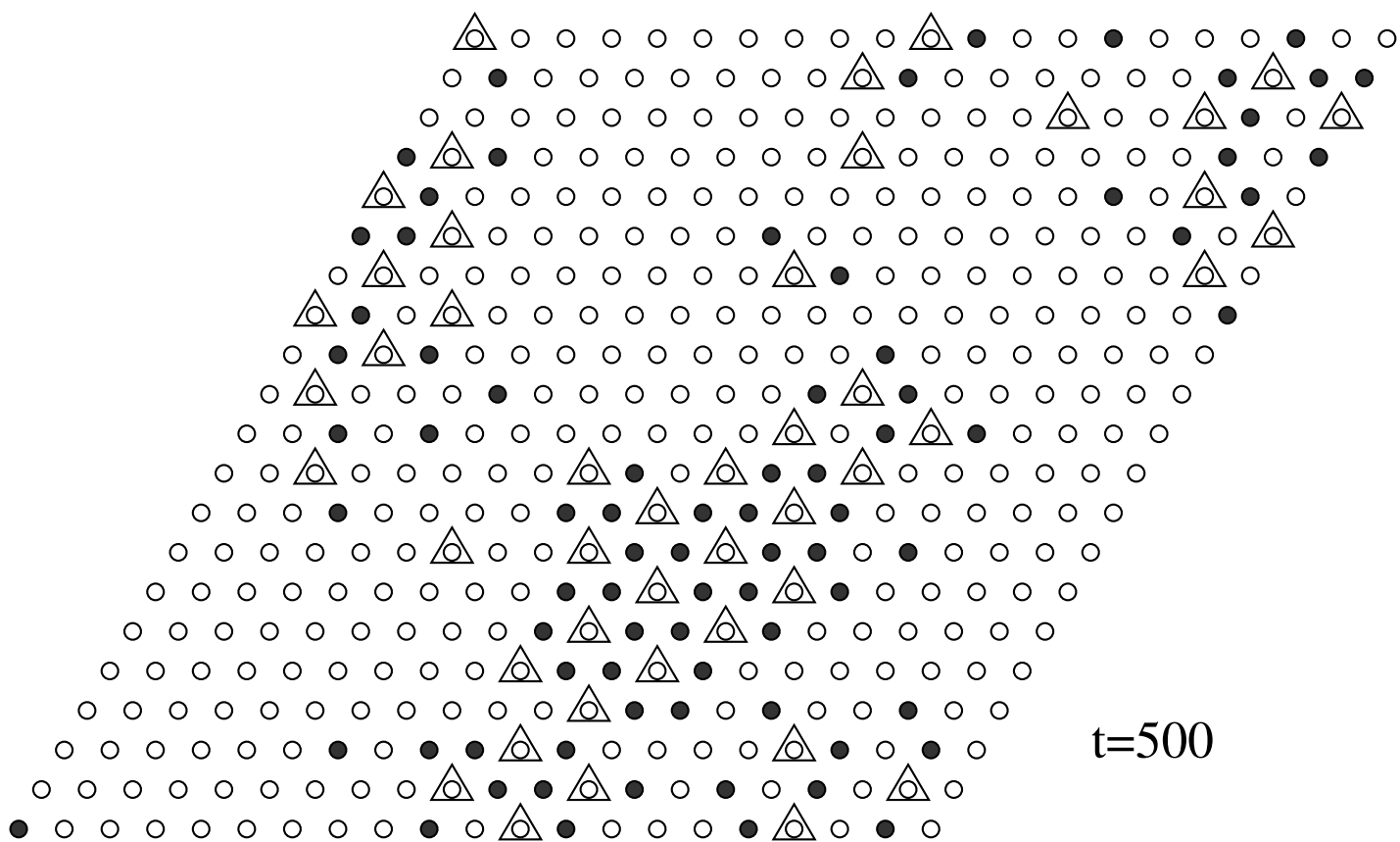




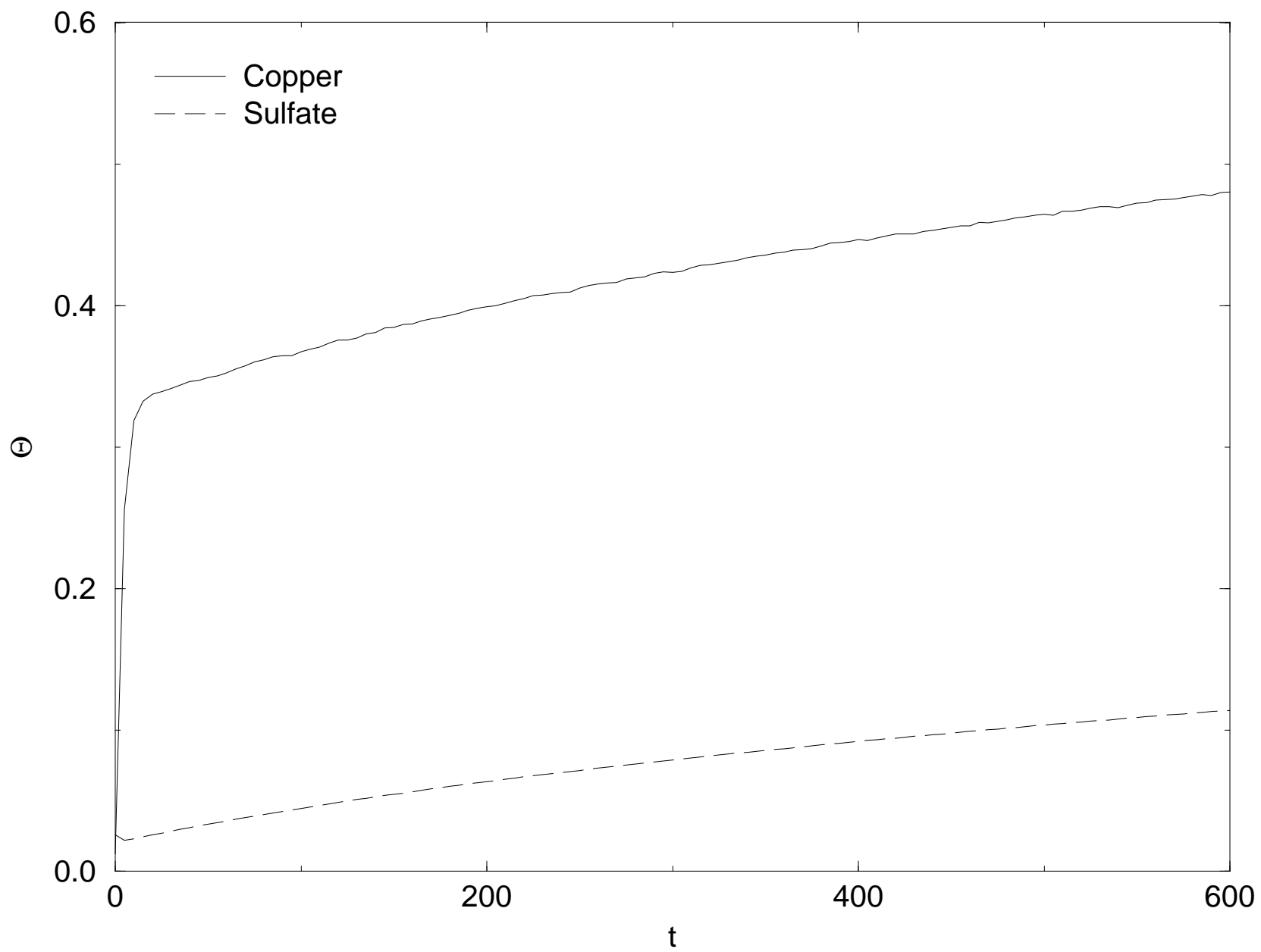


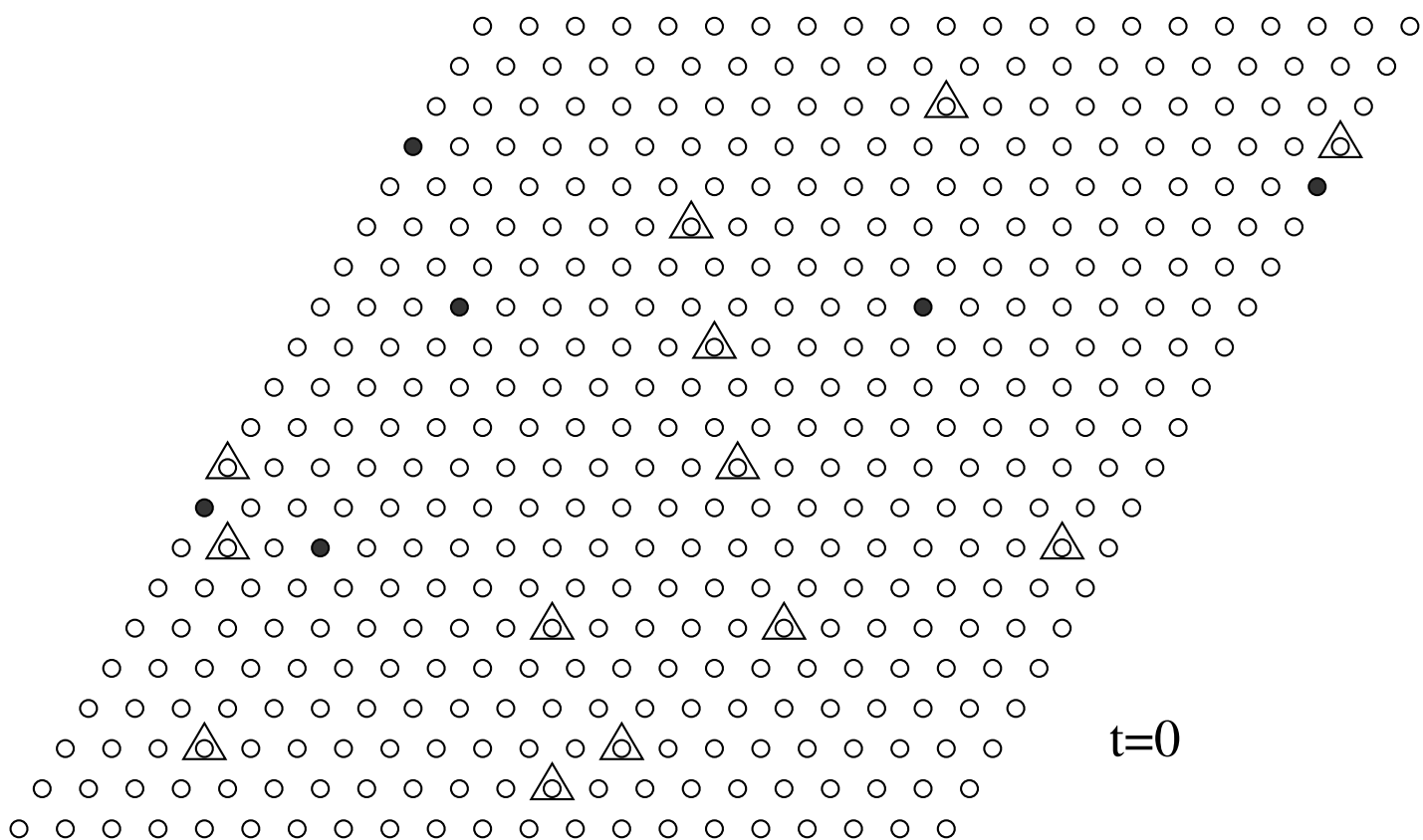


t=300

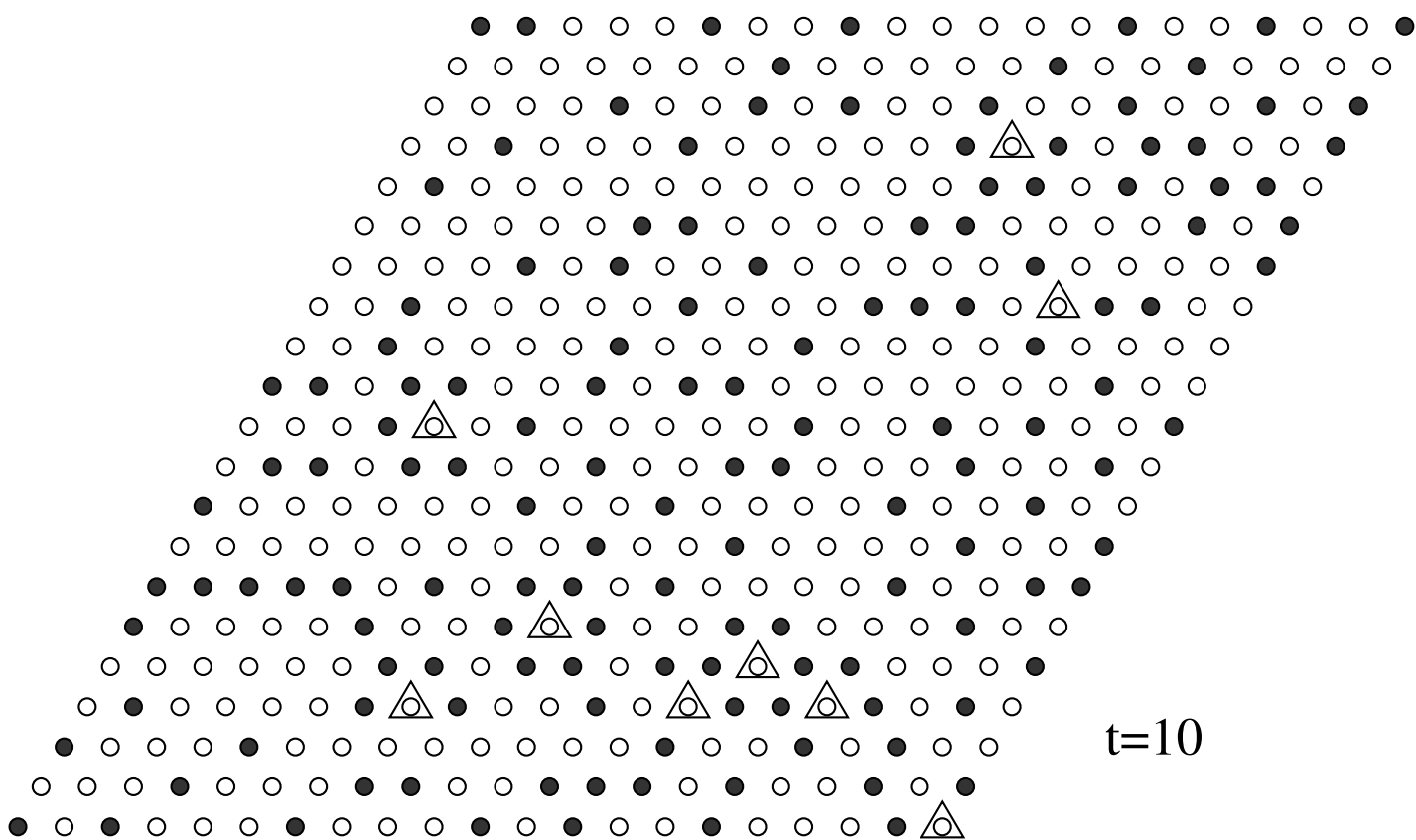


t=500

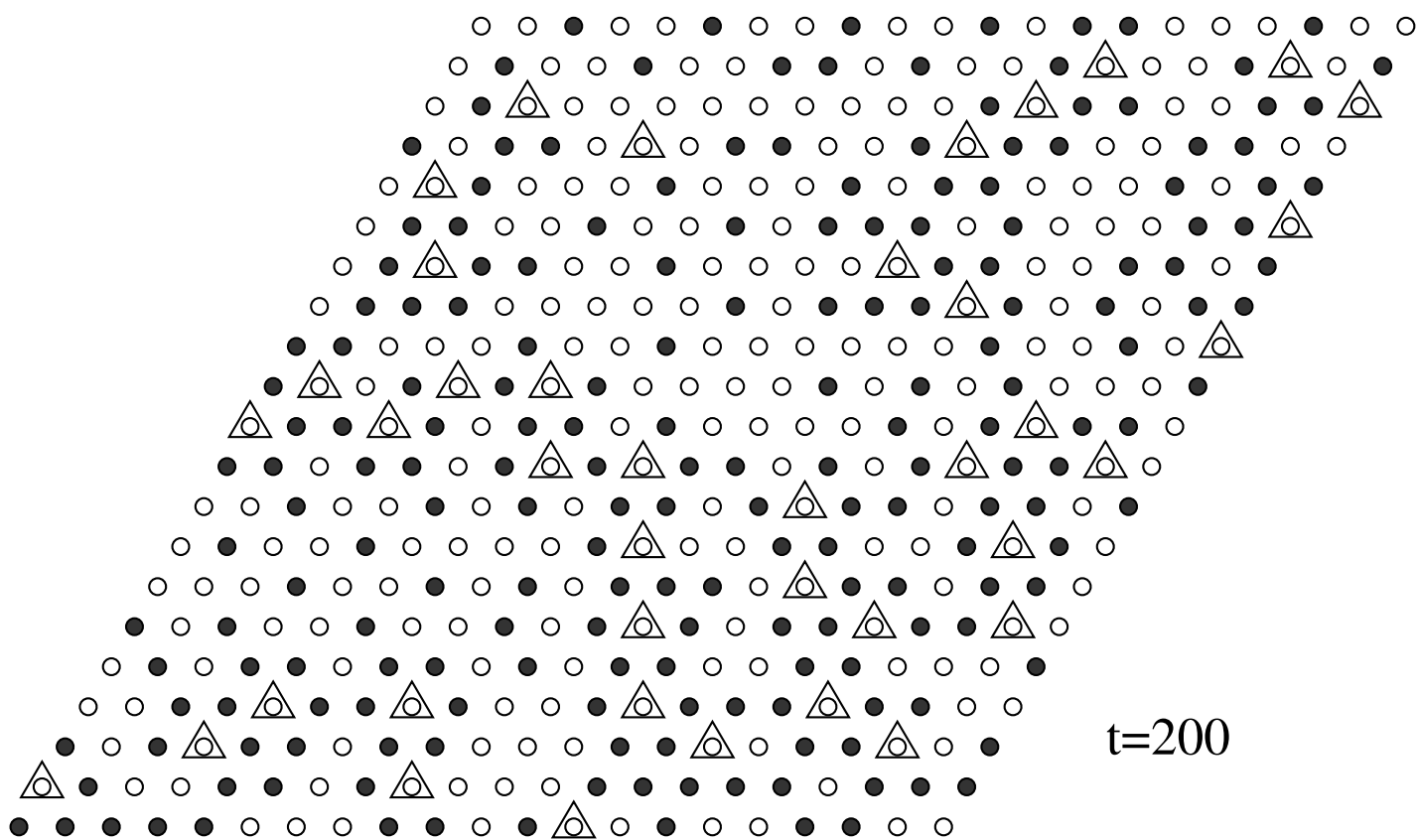




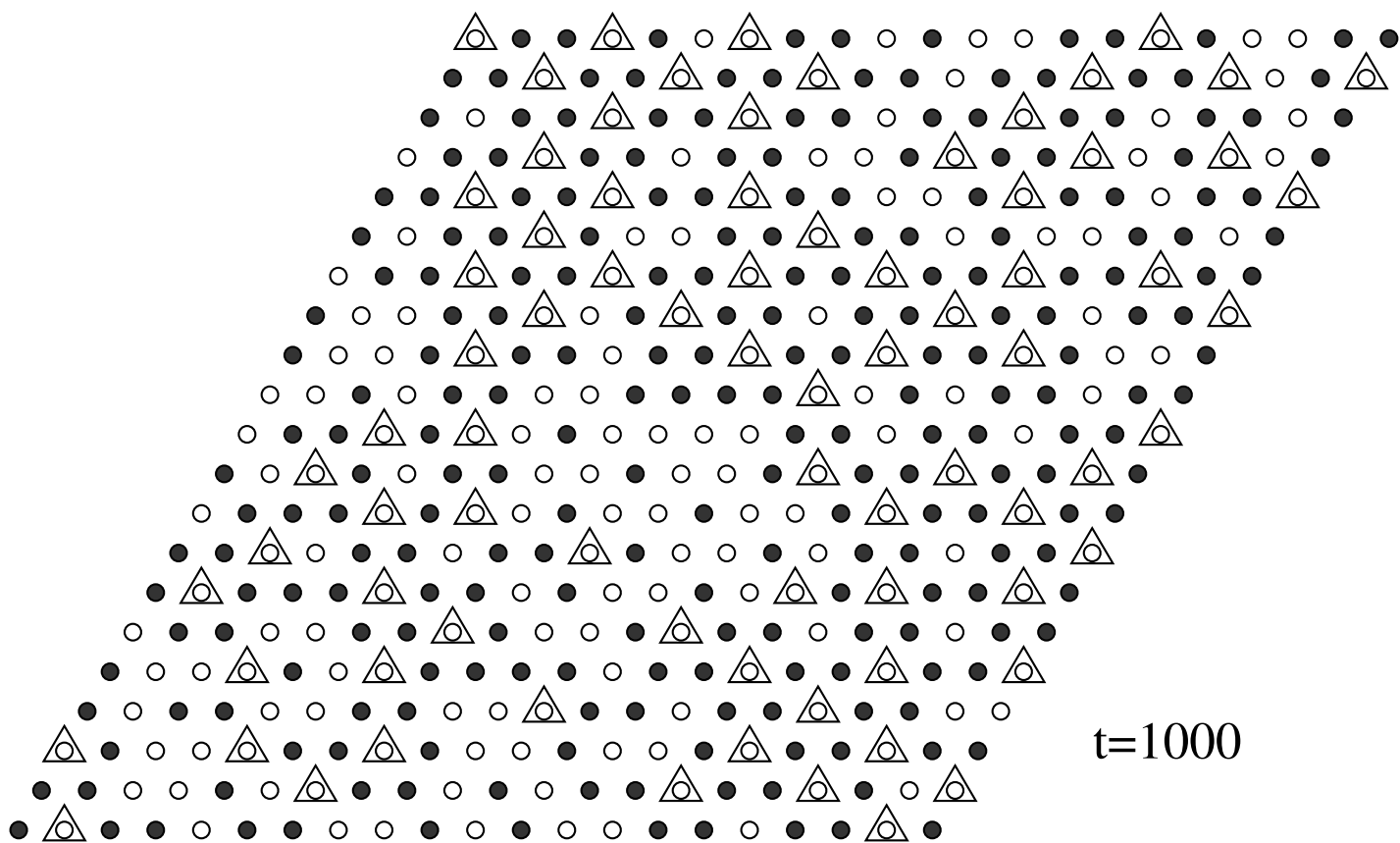
t=0



t=10



t=200



$t=1000$